Turbulent wedge modeling in intermittency-based transition models at high Reynolds numbers

Michael Fehrs

Institute of Aeroelasticity, German Aerospace Center, Bunsenstr. 10, Göttingen, 37073, Germany

A R T I C L E   I N F O

A B S T R A C T

This article presents an approach to set turbulent wedges and transition trippings in local correlation-based intermittency transport transition models. Turbulent wedges are created by increasing the intermittency at the wedge apex or the tripping location. Downstream, no further interference with the transition model is required. The method is demonstrated for the NASA CRM-NLF configuration in a transonic high Reynolds number flow. Prior research on this and other configurations has already shown the important influence of turbulent contamination and boundary layer trippings on the overall aerodynamics. Turbulent wedges and a tripping along a polyline are successfully created for two different intermittency transport models. It is observed that the wedge angles are too large compared to the experimental data. Grid spacing, initial disturbance size, and scaling of the diffusion term only have a minor effect on the wedge angles. This indicates the need to improve the overall transport behavior of the intermittency transport equation for three-dimensional flows. Reynolds number effects are investigated to demonstrate limits of the approach as the transition model gets less sensitive to local disturbances for decreasing Reynolds numbers. In addition to steady transonic flows, the method is also shown for an unsteady transonic flow.

1. Introduction

This article presents a numerical approach to model turbulent wedges and, more general, transition trippings in computational fluid dynamics (CFD) Reynolds-averaged Navier-Stokes (RANS) computations with correlation-based intermittency transport transition models [1,2]. Transition models based on an intermittency transport equation in combination with linear eddy-viscosity turbulence models are favored due to their efficiency. The approach presented here is thought to be applicable to any intermittency transport transition model, e.g. [3–6]. The development of the turbulent wedge approach stems from the requirement to model laminar wind tunnel experiments at high Reynolds numbers in greater detail and to provide a more realistic assessment of future eco-efficient aircraft.

Surface imperfections or surface contaminations result in turbulent wedges in high Reynolds number wind tunnel tests. An example for turbulent wedges in a wind tunnel experiment on a forward swept laminar wing at $M = 0.78$, $Re = 16 \cdot 10^6$ [7] is shown in Fig. 1. Transition is detected based on temperature sensitive paint measurements (TSP) [8]. The transition location is found where the measured light emission
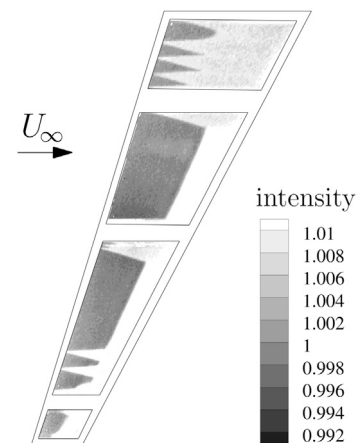

Fig. 1. Transition location and turbulent wedges on a forward swept laminar wing measured with temperature sensitive paint.

intensity increases. A number of turbulent wedges is clearly visible especially on the most inner TSP measurement field.

E-mail address: michael.fehrs@dlr.de.

These wedges can obscure the natural transition location and change the local flow characteristic (e.g. separation location, shock position), which is especially the case once multiple turbulent wedges coalesce further downstream [9]. Although the natural transition location found in an experiment, discarding all turbulent wedges, might still be used for validation purposes for cases with moderate turbulent contamination, computations targeting at a precise prediction of aerodynamic forces can considerably deviate from experimental measurements, when turbulent wedges are not included in the CFD simulation. The inclusion of turbulent wedges is a prerequisite to further validate and improve transition models based on high Reynolds number wind tunnel data.

The same holds for the effect of a transition tripping: the boundary layer in an experiment is usually tripped close to the leading edge to avoid additional Reynolds number effects. Especially at higher angles of attack, it can be important to include the laminar flow up to the tripping location [10]. For laminar wing testing, the laminar boundary layer on the pressure surface is often tripped as no transition detection is employed (e.g. due to limited optical access to the test section) and the pressure surface is often not considered for laminar flow anyway. As the tripped boundary layer will have a larger displacement thickness, the overall flow characteristics on the wing will be affected. The trailing edge flow is only computed correctly if the development of the boundary layer is modeled accordingly.

In addition to wind tunnel testing, the inclusion of turbulent wedges in CFD simulations can support the assessment of natural laminar flow (NLF) transport aircraft configurations. Computations with a randomized turbulent wedge distribution can help to understand the net benefit of laminarization for the overall flight mission. Furthermore, the criticality of certain flow conditions with a local loss of laminarity can be modeled with a numerical tripping as the boundary layer state affects the shock and separation behavior.

A first description of turbulent wedges in a wind tunnel experiment is given by Charters [11]. An early detailed examination of turbulent contamination is given by Schubauer & Klebanoff [12]: a turbulent wedge has a fully turbulent core growing at a half-angle of about 6.4°. The turbulent core is surrounded by an intermittent flow region increasing the wedge half-angle to about 10.6°. Turbulent wedge half-angles for zero-pressure gradient flows are consistently reported by other authors. The half-angles of turbulent wedges [13] and turbulent spots [14] increase for adverse pressure gradients and decrease for favorable pressure gradients.

The exact mechanisms of the lateral spreading of turbulent wedges are still subject of numerical and experimental investigations [15,16]: the growth of turbulent wedges is likely caused by the creation of high- and low-speed streaks on the lateral edges of the wedge in a self-regenerating mechanism. This supports early observations that the lateral growth of turbulent wedges is not driven by turbulent mixing/entrainment alone but by some additional destabilizing mechanism [17].

These specific growth mechanisms of turbulent wedges are beyond the modeling depth of an eddy viscosity model, but an attempt is made in this work to model the lateral spreading by the transport behavior of the intermittency transport equation itself. At high Reynolds numbers, correlation-based transition models can undergo a sudden onset and subsequent transition to turbulence at the slightest increase in pressure [18]. This sensitivity can be exploited to model turbulent wedges by forcing an intermittency value of $\gamma = 1$ locally at the wedge apex or the tripping location. Preliminary steady results for the turbulent wedge tripping have been shown at the STAB Symposium 2022 [19].

The turbulent wedge modeling approach is shown for the Common Research Model natural laminar flow (CRM-NLF) configuration [20] in this paper, for which detailed experimental data is available [21–26]. Section 2 of this article describes the method and its implementation in the DLR TAU-Code [27], Sec. 3 presents various results for the CRM-NLF configuration including grid and parameter studies for steady and unsteady flows, and Sec. 4 draws a conclusion and points out possible future work to further improve intermittency transport transition models.

2. Methods

2.1. CFD solver and specific solver settings

The DLR TAU-Code [27] is used in this investigation. The turbulent wedge method and the transition tripping are developed and tested for the γ transition model [1] and the DLR γ transition model[1] [2]. Both transition models are used in combination with the SST k-ω turbulence model [28].

A central scheme with artificial matrix dissipation [29] is used for the convective flux discretization of the mean flow equations in all computations. The convective fluxes of the turbulence equations are discretized with a second-order Roe upwind scheme. A local time step is used in combination with an implicit Backward-Euler scheme to accelerate convergence employing an LU-SGS scheme [30] for the steady computations. A dual time stepping scheme [31] is used for the unsteady computations.

2.2. Intermittency transport transition models

Intermittency transport transition models use the intermittency γ as a blending variable for the underlying turbulence model. In the case of a combination with the SST k-ω turbulence model, the intermittency γ is used to deactivate the production of turbulent kinetic energy k in the laminar boundary layer with an intermittency value of $\gamma \approx 0$. An intermittency value of $\gamma = 1$ results in the normal turbulence model behavior. The coupling is achieved by modifying the transport equation for the turbulent kinetic energy of the turbulence model [2]:

$$\frac{\partial \rho k}{\partial t} + \frac{\partial \rho u_j k}{\partial x_j} = \widetilde{P}_k - \widetilde{D}_k + \frac{\partial}{\partial x_j}\left[\left(\mu + \sigma_k \mu_t\right)\frac{\partial k}{\partial x_j}\right] \tag{1}$$

with the modified production and destruction terms

$$\widetilde{P}_k = \gamma P_k, \tag{2}$$

$$\widetilde{D}_k = \min\left[\max\left(\gamma, 0.1\right), 1.0\right] D_k. \tag{3}$$

Both transition models are based on the intermittency transport equation of the $\gamma - Re_{\theta t}$ transition model [32]:

$$\frac{\partial \rho \gamma}{\partial t} + \frac{\partial \rho u_j \gamma}{\partial x_j} = P_\gamma - E_\gamma + \frac{\partial}{\partial x_j}\left[\left(\mu + \frac{\mu_t}{\sigma_f}\right)\frac{\partial \gamma}{\partial x_j}\right] \tag{4}$$

with $\sigma_f = 1$, a production term P_γ, and a destruction term E_γ. The production term P_γ for both models reads [1,2]:

$$P_\gamma = F_{length}\,\rho S F_{onset}\left(1 - \gamma\right) \tag{5}$$

with $F_{length} = 14$. The term F_{onset} includes the transition correlation, which differs for both models: while the γ model is solely based on experimental data, the DLR γ model is based on a simplified Arnal-Habiballah-Delcourt (AHD) transition criterion [33,34]. As the AHD criterion is based on a linear stability theory database derived from N-factor curves computed for self-similar Falkner-Skan velocity profiles [34], it is assumed that the DLR γ model has a broader applicability and validity than the γ transition model.

The destruction term D_γ for both models reads [1,2]:

$$D_\gamma = c_{a2}\,\rho\,\Omega\gamma F_{turb}\left(c_{e2}\gamma - 1\right) \tag{6}$$

with $c_{a2} = 0.06$ and $c_{e2} = 50$. For the γ transition model, the term F_{turb} is extended to prevent intermittency destruction in wake regions [1]. Other than that, the definition of D_γ is identical for both models.

---

[1] The former working title of the DLR γ transition has been γ-CAS transition model.
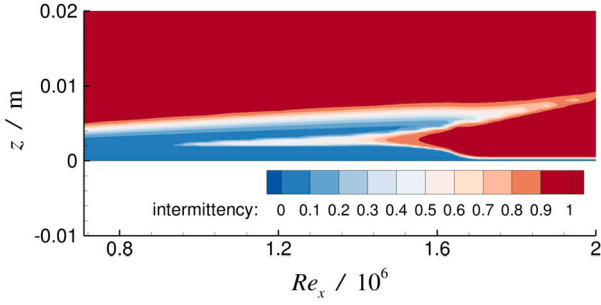
Fig. 2. Intermittency distribution at the transition onset location without any numerical tripping applied.

Fig. 3. Disturbance location $P(x_j)$ and disturbance radius δ_r to determine γ_w.

The details of the specific transition model terms can be found in the corresponding publications [1,2]. For the following discussion it is more important to stress that both models are expected to act identically once the transition onset is forced at the same location. This is due to the fact that the production, destruction, and diffusion terms of the intermittency transport equation are the same for both models.

2.3. Numerical transition tripping

As described above, the intermittency γ in intermittency transport transition models serves as a blending variable for the underlying turbulence model, disabling turbulence production in laminar boundary layer regions. Once the transition criterion is fulfilled, the intermittency production increases and exceeds the destruction term eventually. Fig. 2 shows an example of the intermittency distribution at the transition onset location without any tripping method applied: once the transition criterion is fulfilled, the intermittency increases inside the boundary layer and eventually spreads over the whole height boundary layer downstream. Outside of the boundary layer, the normal turbulence model behavior is recovered with intermittency values of $\gamma = 1$.

At low Reynolds numbers, the intermittency increase for the original intermittency transport models will occur over some distance along the boundary layer resulting in a certain transition region. This transition region is defined as the streamwise length in which the intermittency spreads over the height of the boundary layer. The numerical transition/blending region should not be confused with an experimental measured transition region. There is not necessarily any significant change in boundary layer properties within this region and the transition process might even stall if the boundary layer enters a favorable pressure gradient region with the transition criterion no longer given. At high Reynolds numbers, γ transition models are prone to complete the transition process over a much shorter distance once the transition criterion is met, e.g. at any local adverse pressure gradient [18]. Often, the intermittency spread across the boundary layer is completed over the length of a single cell for these high Reynolds number flows.

This sensitivity at high Reynolds numbers can be used to model turbulent wedges by tripping the boundary layer at the wedge apex without any further prescription of the downstream wedge properties. The tripping is achieved by increasing the intermittency locally and thereby forcing the transition to turbulence. As turbulent wedges are foremost a high Reynolds number phenomenon, the development is solely focused on such flows. As the Reynolds number is decreased, a stronger disturbance might be required to create a turbulent wedge.

The intermittency at specific grid points within the laminar boundary layer is increased to initiate the downstream transition to turbulence. These disturbances are defined by a disturbance location at point $P(x_j)$ and a disturbance radius δ_r, see Fig. 3. This disturbance might represent the apex of a turbulent wedge or a transition tripping. The intermittency at each point $Q(x_j)$ within the disturbance radius is set to $\gamma_w = 1$ based on the distance to the disturbance $\overline{PQ} = |\vec{r}|$:
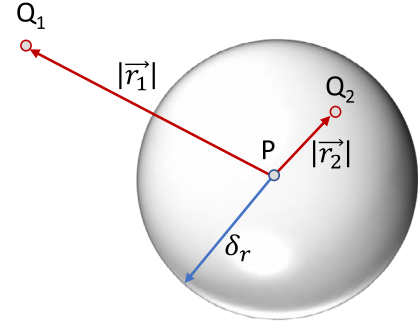
$$\gamma_w(Q) = \begin{cases} 1, & \text{if } |\vec{r}| \leq \delta_r, \\ 0, & \text{if } |\vec{r}| > \delta_r, \end{cases} \tag{7}$$

$$\gamma = \min\left(\max\left(\gamma, \gamma_w\right), 1\right). \tag{8}$$

Fig. 4 shows the surface mesh on a wing with grid points that are flagged turbulent in red. For one of these disturbance locations, the spherical disturbance is shown in blue. It should be noted that the actual tripping is caused by points set turbulent with an intermittency value of $\gamma_w = 1$ in the boundary layer within the spherical disturbance. The application of a sphere allows to use surface coordinates to define the disturbance. The disturbance radius itself is case dependent. It should be chosen as small as possible but must be larger than half the maximum surface grid spacing s_{max}:

$$\delta_r/s_{max} > 0.5. \tag{9}$$

For most RANS model computations of flows over finite wings or aircraft configurations, the spanwise and chordwise grid spacing is in general larger than the wall normal spacing. Therefore, it is assumed that a significant number of points in the boundary layer is flagged turbulent once a surface grid point is located within the disturbance. Equation (9) provides an initial value to define the disturbance radius. In the case of a grid convergence study for which $s_{max} \to 0$, an additional bound for δ_r given by the local boundary layer thickness δ_{99} can be considered to avoid the grid dependency given by Eq. (9):

$$\delta_r/\delta_{99} > 1. \tag{10}$$

Although the transition onset of the unmodified model occurs at some grid points within the boundary layer as shown in Fig. 3, a disturbance that covers the whole boundary layer height will provide a more robust setup. The boundary layer thickness δ_{99} can be estimated e.g. based on the Blasius boundary layer for the local streamwise distance $x_s = l$ or based on the characteristic length $L = l$ of the flow [35]:

$$\delta_{99} \approx 5\sqrt{\frac{\nu l}{U_\infty}}. \tag{11}$$

In addition to a spherical disturbance, a transition tripping along a polyline is implemented. If a given point is located within the disturbance radius around any line segment of the polyline, the point is set turbulent with $\gamma_w = 1$. Grid points within the disturbance are identified in a pre-processing step and γ_w is set for the whole solver run based on the grid point identification number. This allows to use mesh deformation without updating the coordinates of the disturbance.

The turbulent wedge model is based on the assumption that the experimental wedge characteristics downstream of the wedge apex can be recovered by the transition model without any further intervention. However, none of the existing transition models are calibrated to include the desired three-dimensional behavior. As the lateral growth of the turbulent wedge is, among other things, controlled by the size of the diffusion term of the intermittency transport equation, the diffusion
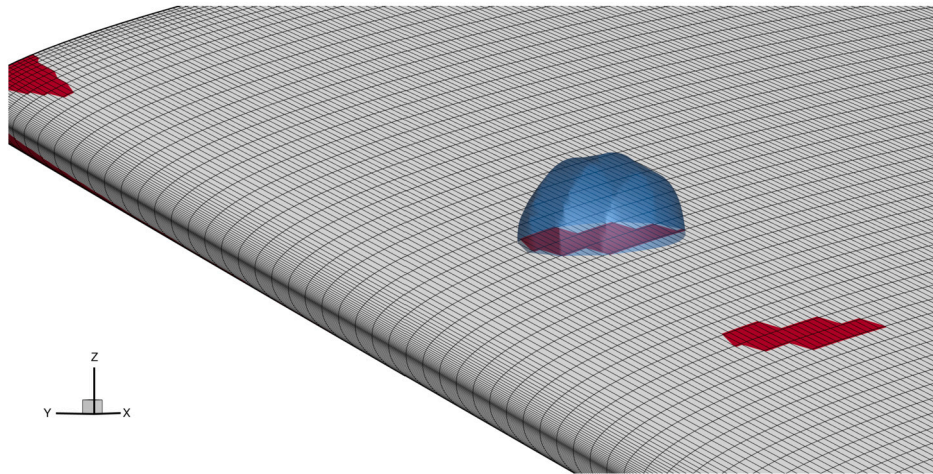
Fig. 4. Surface grid points flagged turbulent (red) and one exemplary spherical disturbance (blue) used to flag the respective points on the surface. (For interpretation of the colors in the figure(s), the reader is referred to the web version of this article.)

term of the transition models is modified by introducing an additional coefficient σ_w:

$$Diff_\gamma = \frac{\partial}{\partial x_j}\left[\sigma_w\left(\mu + \frac{\mu_t}{\sigma_f}\right)\frac{\partial \gamma}{\partial x_j}\right]. \tag{12}$$

The original γ and DLR γ transition models are recovered for $\sigma_f = \sigma_w = 1$. It is assumed that a scaling based on σ_w has a larger effect on the wedge angle as the eddy viscosity vanishes in the laminar boundary layer region at the wedge edge. Any change in model coefficients can have a severe impact on the overall predictive capabilities as local correlation-based transition models are calibrated precisely. The introduction of σ_w with any specific value is solely thought to serve as a parameter to investigate the effect on the turbulent wedge characteristics and no general model improvement is sought. Therefore, a value of $\sigma_w = 1$ is recommended in general to preserve the overall transition model characteristics.

In addition to the behavior of the intermittency transport equation itself, the underlying turbulence model is likely to have an effect on the lateral growth of the turbulent wedges as the intermittency transport equation is affected by the turbulence production itself. The present study is solely focused on the combination with the SST k-ω turbulence model.

2.4. Computational grids

Centaur™ V16.0 by CentaurSoft [36] is used to build two grid families for the CRM-NLF configuration with a gradually varying grid spacing in spanwise and chordwise direction on the wing surface. The hybrid grids consist of a structured quadrilateral surface mesh on the wing and an unstructured triangular mesh on the wing tip, fuselage, and belly fairing. A hexahedral and a prismatic boundary layer grid with nominally 90 layers are created upon the respective structured and triangular surface mesh.[2] The remaining flow field is meshed with tetrahedral elements growing in size towards the far field. The hemispherical far field boundary is approximately 100 wing semi-spans away from the aircraft. The same parametric settings are kept for all grids, but the number of surface grid points in the structured surface grid is changed. The first cell height results in $y_{\max}^+ < 0.62$ for all computations presented in this paper including the Reynolds number variation.

To tell the grids apart, a grid ID is defined. The grid ID is given by: *spanwise no. grid points − chordwise no. grid points*. It will be used

Table 1
Variation of spanwise number of grid points for the grid family with 300 chordwise grid points.

ID	spanwise no. grid points	η_{LE}	N
450 − 300	450	0.25%	30 706 436
550 − 300	550	0.20%	36 327 531
650 − 300	650	0.17%	41 960 529
750 − 300	750	0.15%	47 712 759

Table 2
Variation of chordwise number of grid points for the grid family with 750 spanwise grid points.

ID	chordwise no. grid points	ξ_{chord}	N
750 − 200	200	0.62%	32 351 176
750 − 300	300	0.37%	47 712 759
750 − 400	400	0.27%	63 967 948
750 − 500	500	0.21%	81 315 564

henceforth to reference the computational grid used in each specific investigation. Table 1 and 2 give the spanwise, chordwise, and total number of grid points N for each member of the grid family with the relative span η_{LE} semi-span and chordwise spacing ξ_{chord} as described in the next paragraph.

The structured surface grid on the wing has a clustering of grid points at the leading and trailing edge and at the wing root and tip. The first cell length and growth rates in chordwise direction at the leading and trailing edge and in the spanwise direction at the wing root and tip are the same for all grid. The spanwise grid spacing η_{LE} in Table 1 is given by the grid spacing at the leading edge in terms of semi-span $b/2 = 1.5745715$ m outside of the clustered regions. The chordwise grid spacing ξ_{chord} in Table 2 is given at the Yehudi break[3] in terms of local chord length outside of the clustered regions. The trailing edge height is meshed with 10 evenly distributed grid points for all grids.

---

[2] Centaur™ reduces the number of layers in regions for which stack collisions occur, e.g. the wing-fuselage intersection.

[3] The Yehudi break is the spanwise station of the kink in the trailing edge, see Fig. 2.1 in [26]. The wing taper changes at this location.
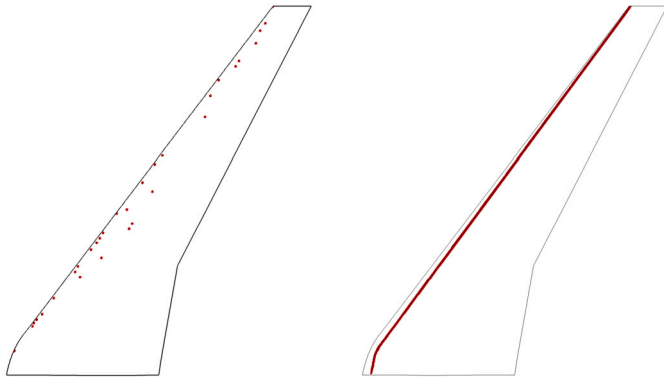
Fig. 5. Turbulent wedge apices on the upper (left) and polyline tripping on the lower (right) wing surface.

3. Results

3.1. CRM-NLF: test case p2523

3.1.1. Test case description

Test case p2523 [37] for the Common Research Model natural laminar flow (CRM-NLF) configuration [20] is used to evaluate the transition tripping method to create turbulent wedges and the polyline tripping. The applicability of the DLR γ transition model has already been shown for this test case [38]. The exact flow conditions as requested for the 1st AIAA Transition Modeling and Prediction Workshop [39] are used to set up the computation:

- $\alpha = 1.44848\,\text{deg}$
- $T_{tot} = 277.10805\,\text{K}$
- $Re_{mac} = 14\,971\,972$
- $M = 0.856489$
- $c_{mac} = 0.3642868\,\text{m}$
- $Tu = 0.24\%$

Helm et al. [9] present an investigation into the effects of static deformation and turbulent wedges on the aerodynamics of the CRM-NLF configuration based on the TAU transition module [40,41]. The TAU transition module includes an e^N method [42] based on linear stability theory for transition prediction. In addition, the TAU transition module allows the definition of arbitrary transition lines. This approach is not directly applicable to the correlation-based intermittency transport transition models in the DLR TAU-Code. The serrated transition front found in the experiment is set by Helm et al. [9] to investigate the effect of turbulent wedges on the aerodynamics. In the present study, only the wedge apices are used to model these turbulent wedges.

3.1.2. Set-up of turbulent wedges and polyline tripping

The surfaces coordinates of the turbulent wedge apices on the upper wing surface are used to define the disturbance locations. The center of the disturbance is located on the wing surface. On the lower surface, a polyline tripping at 5% of the local chord is applied. For both, the turbulent wedges and the polyline tripping, a disturbance radius of $\delta_r = 0.005$ m is used. The computations are performed on grid ID $550 - 300$. Fig. 5 shows the wedge apices on the upper side and the polyline on the lower side of the wing.

Fig. 6 shows surface grid points that are flagged turbulent. In Fig. 6a) the tripping at two wedge apices is shown. For a disturbance radius of $\delta_r = 0.005$ m, three spanwise rows of surface points are flagged turbulent spanning about 0.0075 m.

For comparison, trip dots of much smaller dimension are used in the experiment on the lower surface of the wing. These dots have a diameter of 0.00127 m ($= 0.05$ in) with an height of only $\approx 5 \cdot 10^{-5}$ m ($= 0.002$ in) [26]. The height of the laminar boundary layer at the wedge

apex location shown in Fig. 6a) is $\delta_{99} \approx 0.0001$ m. Thus, the hemispherical extent of the numerical tripping into the flow domain is too large compared to the boundary layer thickness. However, the disturbance size is mainly determined by the spanwise grid spacing as some points need to be flagged turbulent. A disturbance size smaller than the spanwise grid spacing might result in no flagged points at all. This indicates a methodical shortcoming as the spanwise grid spacing has in general the coarsest grid resolution. A more complex flagging algorithm based on a nearest neighbor search for a given location might be useful for further consideration.

Another methodical shortcoming is shown in Fig. 6b) and 6c): the disturbance radius of $\delta_r = 0.005$ m for the polyline tripping on the lower surface intersects the upper surface so that points are flagged turbulent in the boundary layer on the upper side of the wing. This will create a spurious turbulent wedge. In this specific case, the effect is negligible as a turbulent boundary layer is found right at the leading edge of the wing tip anyways. A future application will need to exclude grid points that are not associated with the boundary layer on a specific surface sought to be tripped by e.g. determining the desired state of the surface boundary marker (e.g. free transition, fully turbulent, tripped).

3.1.3. Results for the basic set-up: turbulent wedges

This section will describe the results for test case p2523 computed with free transition and with turbulent wedges and polyline tripping for the γ and DLR γ transition models. Although the boundary layer transition location is free to move between wedges, the set-up with wedges and polyline will be referred to as *tripped* further on. The results will be compared with results by Helm et al. [9] computed with the TAU transition module with free boundary layer transition and with the prescribed transition front found in the experiment. In the free transition computations with the e^N method based on linear stability theory in the TAU transition module, the transition prediction is only performed on the upper surface. The boundary layer on the lower surface is tripped at the experimental tripping location (i.e. 5% local chord length) [9]. The present free transition computations with the correlation-based transition models have no tripping on the lower surface. No detrimental effect on the solver convergence is observed, when the turbulent wedge tripping is applied.

Fig. 7 shows the skin friction coefficient (c_f) distribution computed with the TAU transition module on the upper surface of the wing excluding the wing tip [9]. The transition location is found at the main increase in c_f. It is marked with a solid black line. The transition prediction based on the e^N method for free boundary layer transition in Fig. 7a) is satisfying considering the experimental transition position seen in Fig. 7b) if the turbulent wedges are disregarded to define the natural transition location in the experiment.

Fig. 8 and 9 show the c_f distribution on the upper surface of the wing computed with the DLR γ and γ transition model, respectively. In Fig. 8a) and 9a), the c_f distribution is superimposed with the transition front (solid black line) computed with the TAU transition module for free boundary layer transition. The free transition computation with the DLR γ transition model agrees well with the TAU transition module results except for the most inner wing. The γ transition model gives a transition position too far upstream from the wing root up to the Yehudi break. This supports the assumption of improved predictive capabilities given by the simplified AHD criterion used in the DLR γ transition model.

Fig. 8b) and 9b) show the results for the tripped computations. The skin friction distributions are superimposed with the experimental transition front. The turbulent wedges are successfully created by the numerical tripping at the wedge apex locations. However, the half-angles of the turbulent wedges are too large compared to the experimental transition front. The experimental half-angles range from $\Lambda/2 \approx 10°$ to $12.5°$. The turbulent wedges predicted by the intermittency transport models are in the range from $\Lambda/2 \approx 17.5°$ to $22.5°$.

Even in regions that are not directly influenced by the turbulent wedges, boundary layer transition is affected as the transition location
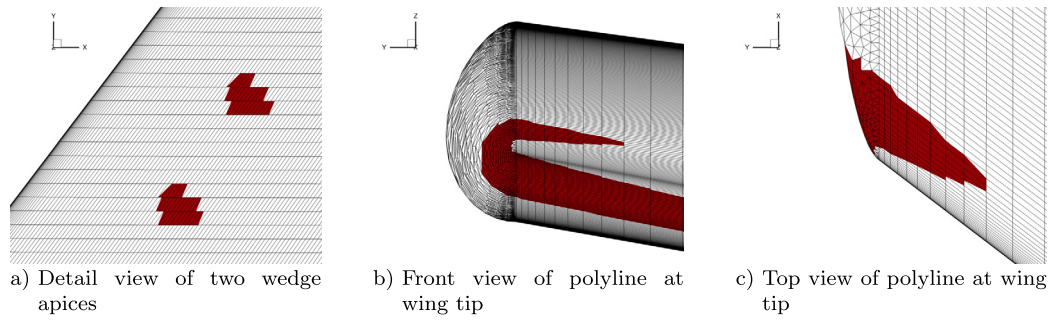
a) Detail view of two wedge apices

b) Front view of polyline at wing tip

c) Top view of polyline at wing tip

Fig. 6. Surface grid points flagged turbulent for wedge apices and polyline at wing tip.

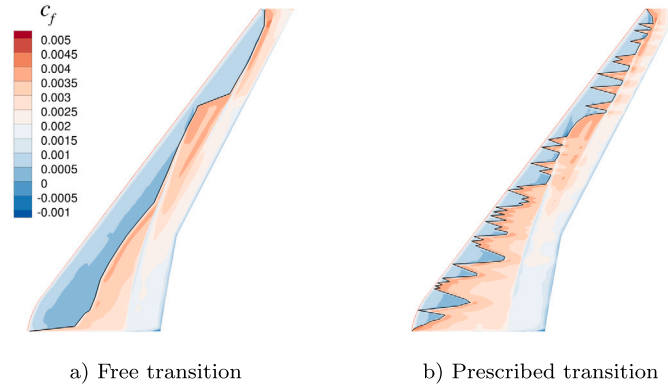a) Free transition

b) Prescribed transition

Fig. 7. TAU transition module results on the upper surface [9] with transition location (solid black line). Transition is prescribed at the experimental transition location including turbulent wedges.
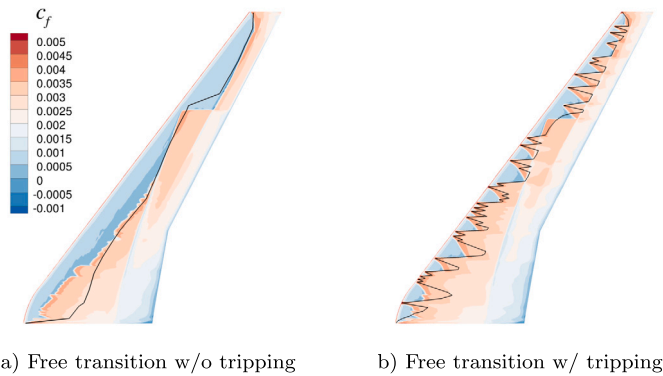

a) Free transition w/o tripping

b) Free transition w/ tripping

Fig. 8. DLR γ transition model results on the upper surface with superimposed transition fronts from [9] (solid black line). The tripping is applied at each wedge apex.

a) Free transition w/o tripping

b) Free transition w/ tripping
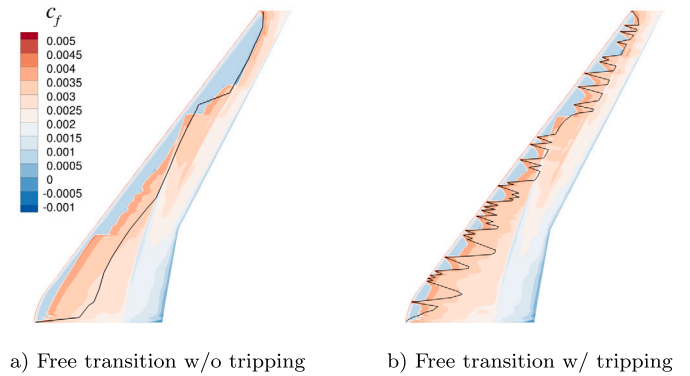
Fig. 9. γ transition model results on the upper surface with superimposed transition fronts from [9] (solid black line). The tripping is applied at each wedge apex.

shifts slightly upstream and for some spanwise stations even downstream between the turbulent wedges. This indicates that the overall aerodynamics of the wing changes as differences in the streamwise pressure gradient shift the transition location.

Fig. 10 gives a detail view of the skin friction and pressure coefficient distribution in the vicinity of turbulent wedges. The superposition with the experimental transition front shows that the wedge edges towards the wing tip are in better agreement than the inner edges. Therefore, the numerical turbulent wedges are oriented in a steeper angle to the leading edge. For the pressure coefficient distribution in Fig. 10b), a zebra shading is used to show how pressure distortions are created at the inboard edge of the turbulent wedge (windward[4]), that is not found at the outboard edge (leeward). Pressure distortions at the transition loca-

tion are usually caused by the sudden change in displacement thickness of the boundary layer.

Fig. 11 shows the intermittency distribution in cut planes along a turbulent wedge. The intermittency covers the whole boundary layer height within a short lateral distance and the skin friction changes accordingly. Therefore, it is justified to use the c_f distribution as a direct measure of the turbulent wedges rather than the intermittency itself. The windward side of the wedge shows a more differentiated distribution of intermittency with an increase originating inside the boundary layer. This intermittency increase spans over some boundary layer cells in lateral direction. On the leeward side of the wedge, the intermittency increase occurs abruptly over the whole boundary layer height and over the length of a single cell.

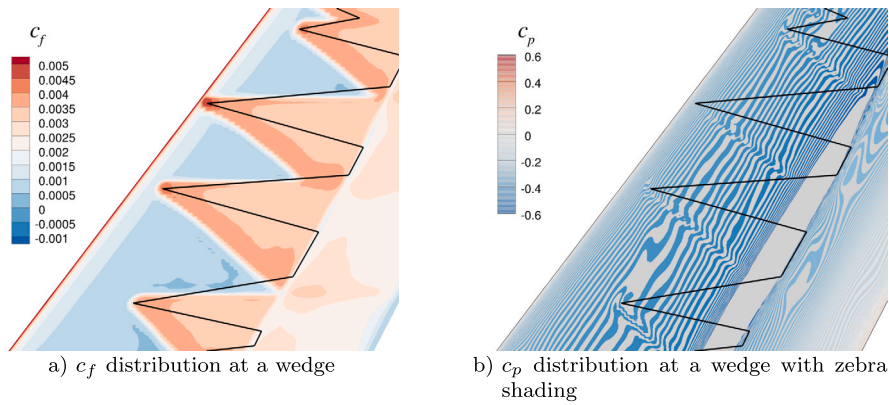[4] w.r.t. local skin friction lines not shown here.

a) c_f distribution at a wedge

b) c_p distribution at a wedge with zebra shading

Fig. 10. Detail view of turbulent wedges computed with the DLR γ transition model.
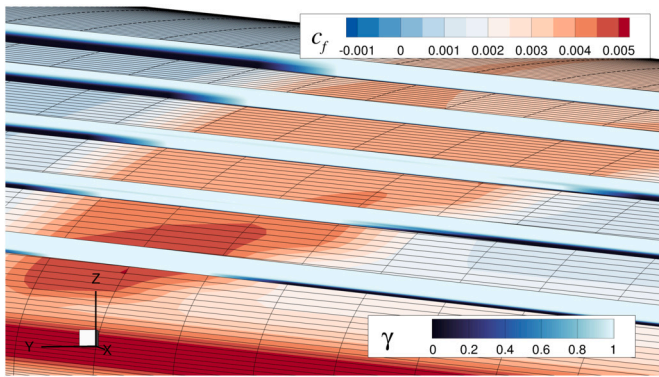

Fig. 11. Intermittency distribution inside the boundary layer along a turbulent wedge.
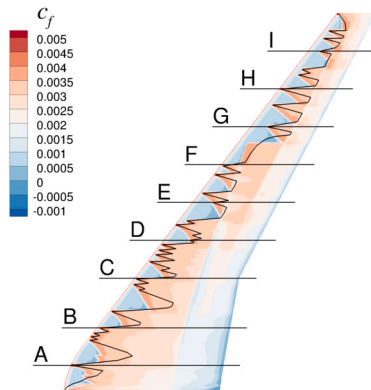

Fig. 12. Skin friction coefficient distribution for DLR γ transition model, experimental transition location (solid black line), and experimental pressure rows A to I.

3.1.4. Results for the basic set-up: effect on aerodynamics

This section will investigate the effect of the turbulent wedges on the aerodynamics. The CRM-NLF wing tested in the NASA Langley National Transonic Facility (NTF) is equipped with 230 static pressure orifices in nine streamwise rows [24]. The surface pressure data is available [25]. The positions of the nine pressure rows are shown in Fig. 12 with the CFD solution given by the DLR γ transition model and the experimental transition location. Most of the pressure rows cause a turbulent wedge.

Fig. 13 shows the experimental and numerical c_p distribution for a free transition computation and the tripped computation for the DLR γ transition model at each pressure row. The corresponding friction coefficient distribution is shown in Fig. 8. The differences between the free and tripped numerical solution increase towards the outer wing as

the relative length of the laminar boundary layer increases. For some pressure rows, an improved or locally improved prediction of the c_p distribution is found (e.g. row G or row F at the second shock). For other pressure rows, the effect on the pressure distribution on the upper surface is detrimental (e.g. row I or row F at the first shock). The pressure distribution on the lower surface is improved for all pressure rows, especially towards the trailing edge, as a large amount of laminar flow occurs without the numerical tripping. Without tripping, transition takes place in the adverse pressure gradient region close to mid-chord on the lower wing surface. The transition location can be identified by a sharp local increase in pressure, e.g. at $x/c \approx 0.45$ in row G.

Fig. 14 shows the effect of different numerical configurations computed with the DLR γ transition model on the aerodynamic coefficients in combination with the experimental data [25]. The numerical configurations include the following set ups:

- *tripped*: a computation with turbulent wedges tripped at the wedge apices on the upper surface and a polyline tripping on the lower surface
- *only polyline*: a computation with free boundary layer transition on the upper and a polyline tripping on the lower wing surface
- *free transition*: a computation with free boundary layer transition on the upper and lower surface with no boundary layer tripping

Overall, there is a strong effect on the aerodynamics if turbulent wedges and/or the tripping on the lower surface of the wing is modeled. The experimental lift coefficient is met best for the tripped configuration. The experimental moment coefficient is in better agreement with the computation that only includes the polyline tripping. For the drag coefficient, there is large gap for either configuration. Considering the results for the free boundary layer transition computation, it is observed that a numerical tripping is a necessary prerequisite to model laminar wind tunnel experiments once the flow is tripped in the experiment on any side of the wing.

3.2. Influence of grid resolution

Figs. 15 and 16 show the skin friction coefficient distribution given by the DLR γ model for the variation of spanwise and chordwise grid spacing as specified in Sec. 2.4, respectively. Only the upper wing surface is shown. The disturbance radius is set to $\delta_r = 0.005$ m. No significant effect of the grid resolution on the turbulent wedge half-angles is observed. The orientation of the turbulent wedges does not change neither. The outboard edges of the turbulent wedges stay aligned with the structured surface grid.

Fig. 17 shows the effect of the grid refinement on the lift and moment coefficient for both transition models. The refinement is described in terms of an equivalent mesh size based on the total number of grid points $1/N^{1/3}$ [43] with finer grids located further left on the abscissa axis. The
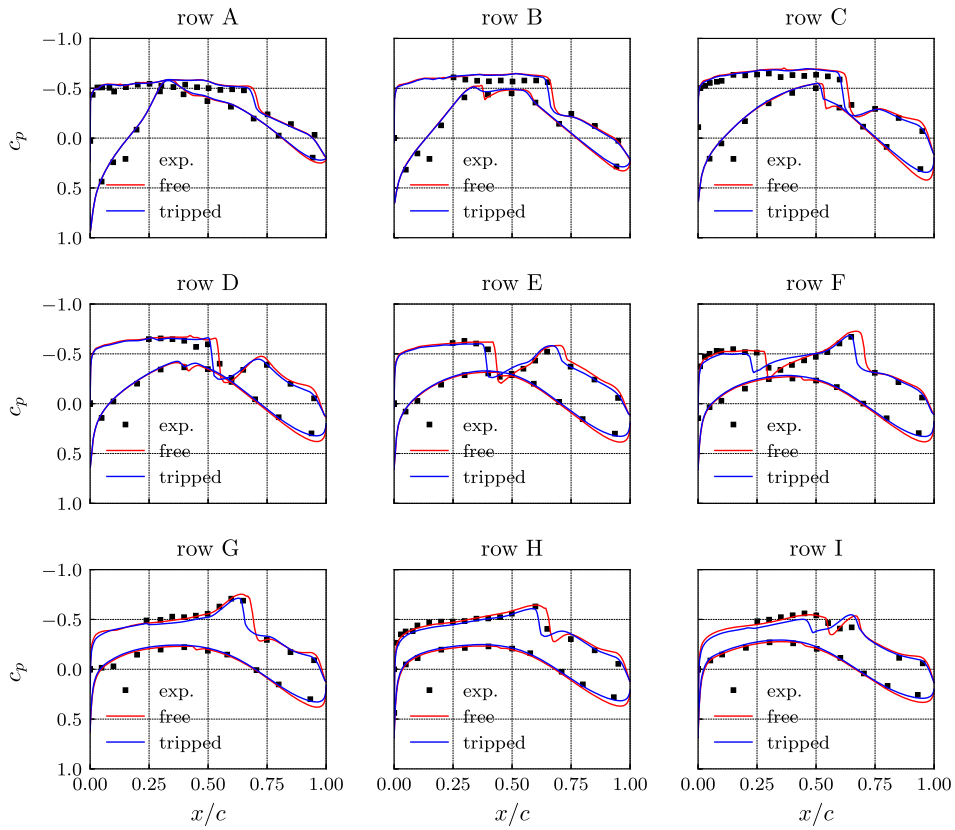
Fig. 13. Experimental and numerical c_p distribution with free and tripped transition for the DLR γ transition model.
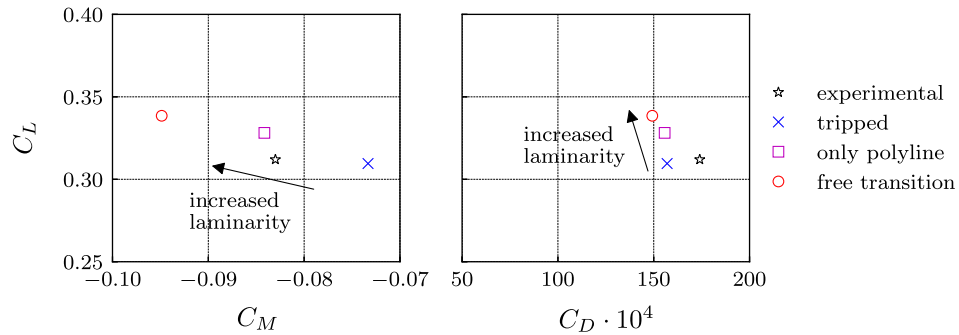

Fig. 14. Aerodynamic coefficients: experimental and numerical for the DLR γ transition model with wedges and polyline (tripped), only polyline tripping, and free boundary layer transition.
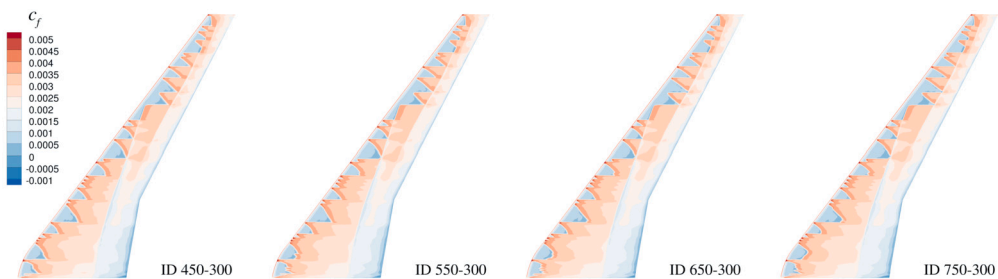

Fig. 15. Effect of spanwise grid spacing on the skin friction coefficient distribution on the upper surface of the wing for the DLR γ transition model.
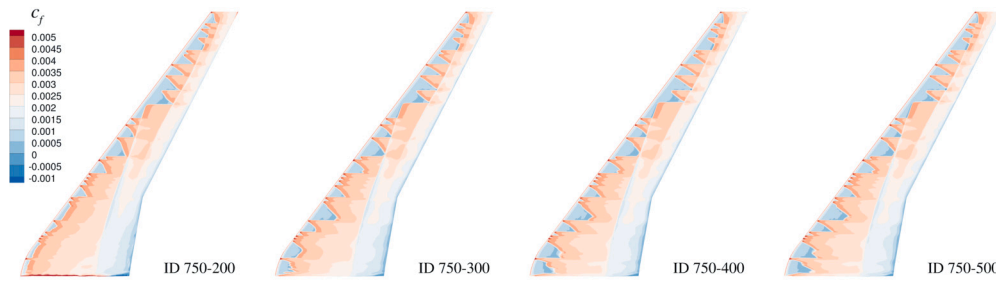
Fig. 16. Effect of chordwise grid spacing on the skin friction coefficient distribution on the upper surface of the wing for the DLR γ transition model.
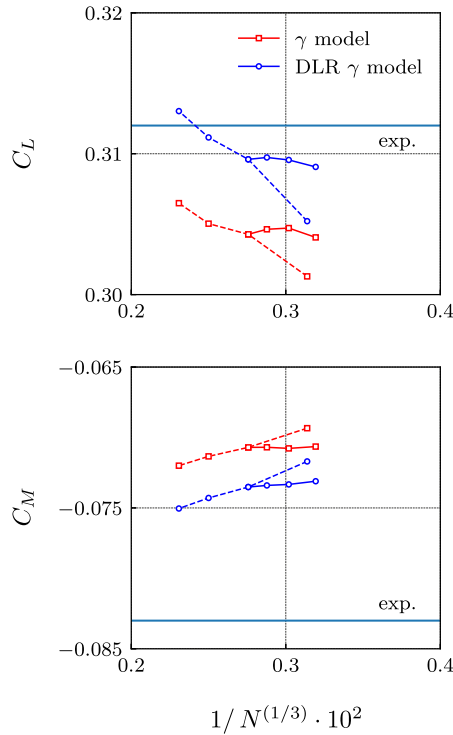

Fig. 17. Effect of grid refinement on the lift and moment coefficient: solid line - spanwise refinement; dashed line - chordwise refinement; horizontal line - experimental value.

solid line shows the spanwise refinement, the dashed line shows the effect of the chordwise refinement. Both transition models show a stronger effect of the chordwise refinement on the aerodynamic coefficients. The more upstream transition location predicted by the γ transition model results in a larger displacement thickness at the trailing edge. Therefore, the lift and moment coefficients differ from the DLR γ model results.

3.3. Influence of disturbance radius

The disturbance radius is changed for the basic test case to investigate the effect on the turbulent wedges. The DLR γ model is used on grid ID $550 - 300$. The results are presented in Fig. 18. For disturbance radii $\delta_r > 0.0015$ m, there is always a grid point located within the disturbance on the given surface mesh. Once the disturbance radius is smaller, a turbulent wedge might not be initialized as it is the case for $\delta_r = 0.001$ m on the outer wing.

The overall effect of a reduced disturbance size is small: the apices of the turbulent wedges are represented better as the disturbance size is reduced, but the orientation of the wedges and the wedge half-angles are not affected. For all disturbance radii in Fig. 18, the spurious wedge at the wing tip does not occur as the disturbance radius connected to the polyline on the lower wing surface does not intersect the upper sur-

face anymore. In consequence, a disturbance radius should be defined to cover at least one grid point on a given surface mesh. This approach might not be suited for lower Reynolds numbers as the transition model is less sensitive to a local increase in intermittency.

3.4. Influence of diffusion coefficients

The diffusion term of both transition models is scaled by the diffusion coefficient σ_f (see Eq. (4)) and in the case of the extended model additionally by σ_w (see Eq. (12)). The original models are obtained for $\sigma_f = 1$ and $\sigma_w = 1$. As the turbulent wedge angles are too large compared to the experimental data, a decrease in diffusion is sought by either increasing σ_f or decreasing σ_w. Fig. 19 shows the effect of σ_w on the skin friction coefficient distribution. The computations are performed on grid ID $750 - 300$ with a disturbance radius of $\delta_r = 0.002$ m. The grid with 750 surface grid point in spanwise direction is chosen to promote any lateral effect of the diffusion behavior on the intermittency distribution.

No significant effect on the lateral growth of the turbulent wedge is observed for a decrease in σ_w, but there is a downstream effect on the skin friction coefficient distribution. The skin friction levels of the original model are not recovered due to the intermittency distribution close to the wall within the turbulent boundary layer. Both intermittency transport models have a vanishing intermittency value directly at the wall in turbulent boundary layers. For the test cases with reduced σ_w, the intermittency stays close to its floor value too far away from the wall, which hinders the development of a turbulent velocity profile. For the increased value of $\sigma_w = 10$, the transition model breaks down as the intermittency shows a stratified distribution in the boundary layer with regions of $\gamma = 1$ alternating with layers of vanishing intermittency. A variation of σ_f is not able to change the wedge angles neither.

For this high Reynolds number flow, the intermittency transport behavior is dominated by advective transport. A further decrease in diffusion is therefore probably not suited to decrease the wedge angles. Future investigations need to show how advected intermittency, production/destruction of intermittency, intermittency distribution, and pressure distortions caused by the initial wedge apex affect the downstream wedge angle.

3.5. Influence of Reynolds number

Fig. 20 shows the skin friction coefficient distribution for a Reynolds number variation. The computations are performed with the DLR γ transition model on grid ID $550 - 300$ with $\delta_r = 0.002$ m. The effect is twofold: firstly, the wedge angles decrease with decreasing Reynolds number. At a mean aerodynamic chord Reynolds number of $Re_{mac} = 8 \cdot 10^6$, the wedge angles are close to the experimental data, but the orientation of the wedges does not improve. In addition, a first wedge (3rd outboard) is not initialized anymore at the lowest Reynolds number. This is an expected effect as the transition model gets less sensitive to a local intermittency increase. Secondly, the free transition location between the wedges moves downstream with decreasing Reynolds number. As $Re_\theta \sim \sqrt{Re_x}$ for a given location x along the boundary layer, the
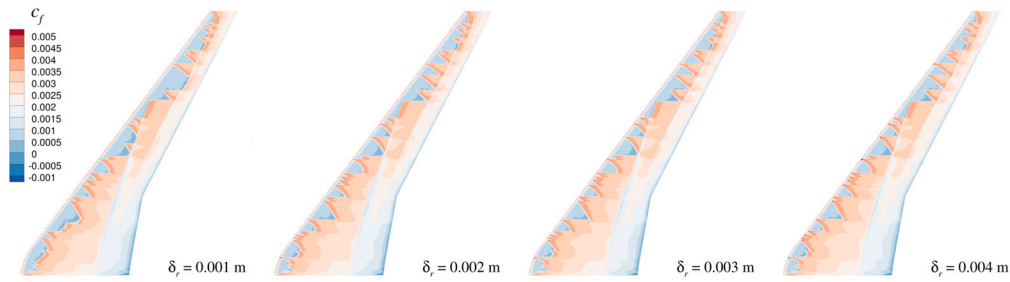
Fig. 18. Influence of the disturbance size on the turbulent wedges on the upper surface of the wing for the DLR γ transition model.
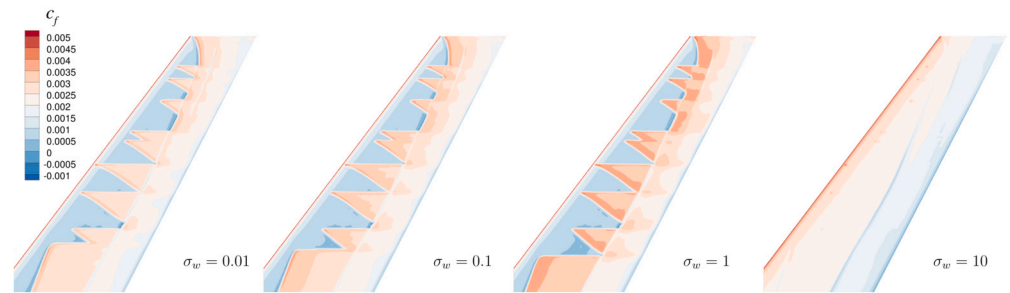

Fig. 19. Influence of σ_w on the turbulent wedges on the upper surface of the outer wing for the DLR γ transition model.
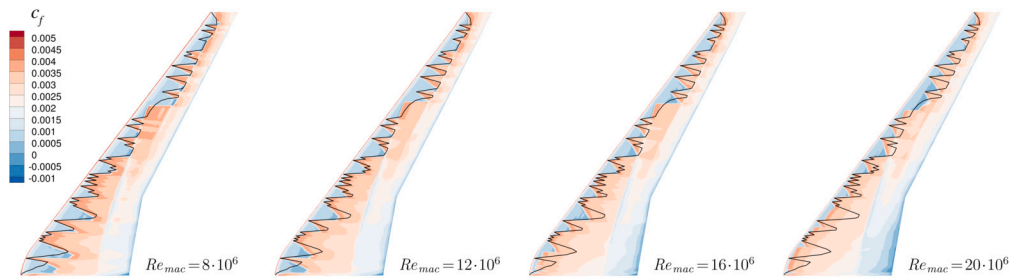

Fig. 20. Influence of Reynolds number on the turbulent wedges on the upper surface of the wing for the DLR γ transition model and experimental transition location for p2523 at $Re_{mac} \approx 15 \cdot 10^6$ (solid black line).
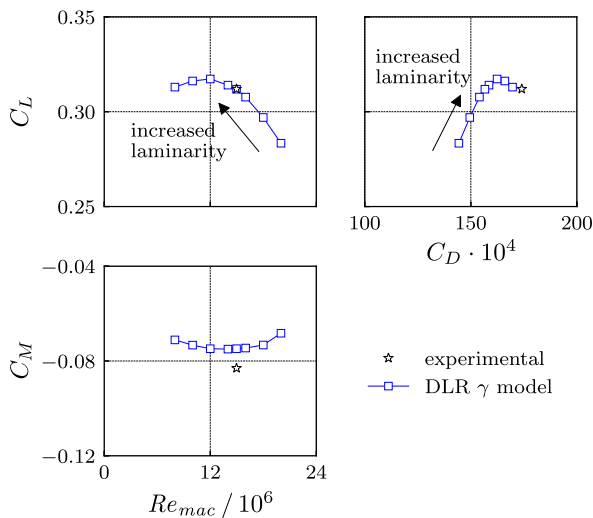

Fig. 21. Influence of Reynolds number on aerodynamic coefficients with tripped boundary layer for the DLR γ transition model.

transition location moves downstream for decreasing Reynolds numbers for a given transition onset momentum thickness Reynolds number $Re_{\theta t}$ defined by the turbulence level, pressure gradient, and Mach number.

Fig. 21 shows the influence of the Reynolds number on the aerodynamic coefficients. Although the amount of laminar boundary layer flow decreases with increasing Reynolds number, the drag coefficient C_D decreases due to the combined effects of a lift decrease on induced drag and the Reynolds number effect on skin friction drag. In fact, the lowest Reynolds number with the largest amount of laminar flow has the largest overall drag coefficient. Although a detailed drag breakdown into its single components is beyond the scope of this paper, the drag variation shows the difficulties in specifying the net benefit of laminar flow technologies if assessed not at the actual flight/design Reynolds number.

3.6. Boundary layer tripping in unsteady flows

The flutter stability of a given structure, e.g. wing or airfoil section, is determined by the unsteady aerodynamic forces [44]. These forces change with the boundary layer state. Dedicated wind tunnel tests are required to validate the predictive capabilities of transition models for unsteady boundary layer transition. To give a better representation of an actual wind tunnel set-up, turbulent wedges and turbulent trippings are likely required in the numerical model.

Based on the flow conditions of the NASA test case p2523, unsteady computations with the CRM-NLF configuration are performed. The tripped case with turbulent wedges on the upper surface and a polyline tripping on the lower surface is compared with a free transition case without any tripping. Mono-frequent pitch motions are
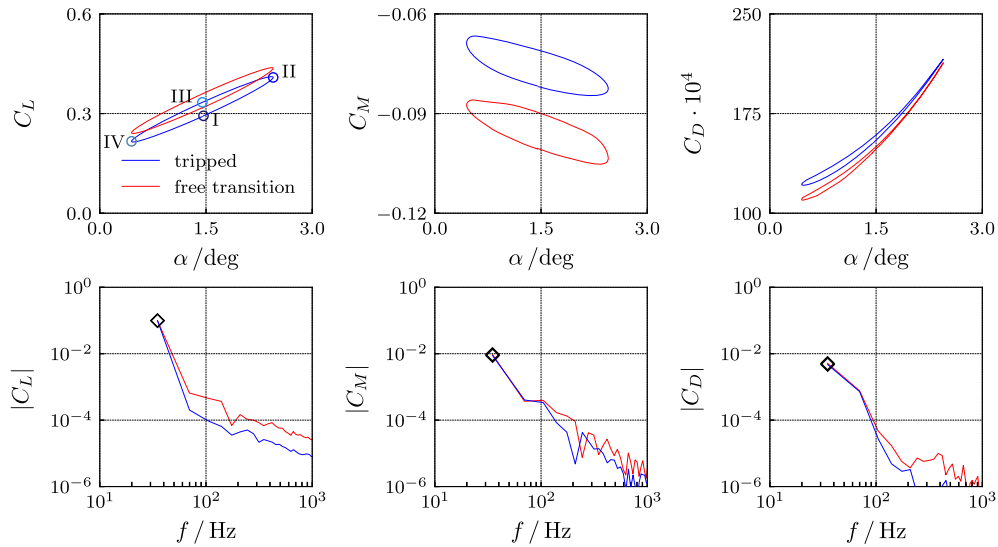
Fig. 22. Unsteady aerodynamic coefficients and respective amplitude spectra for one pitch period at $k = 0.15$ with tripped and free boundary layer transition.
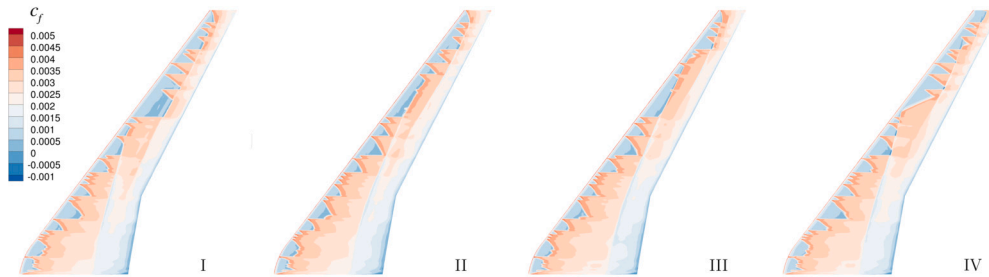

Fig. 23. Instantaneous c_f distribution during the pitch cycle for the DLR γ transition model at $k = 0.15$ with tripped boundary layer transition.
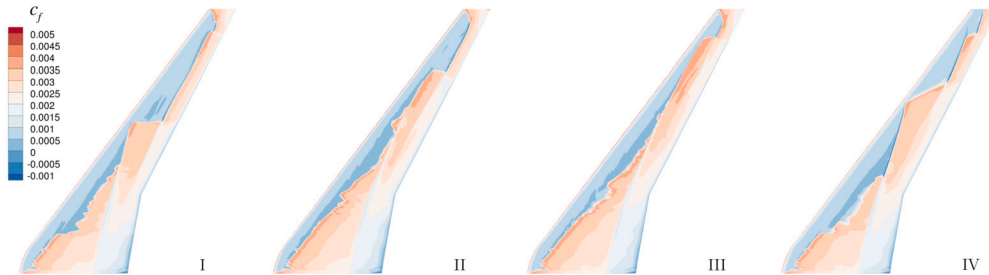

Fig. 24. Instantaneous c_f distribution during the pitch cycle for the DLR γ transition model at $k = 0.15$ with free boundary layer transition.

computed for different reduced frequencies $k = (\pi f\, c_{mac})/U_\infty$ with a pitch amplitude of $\hat{\alpha} = 1\,\mathrm{deg}$ about the moment reference center at $(1.7512284\,\mathrm{m}, 0\,\mathrm{m}, 0.2350516\,\mathrm{m})$. The computations are performed with the DLR γ transition model on grid ID $550-300$. A disturbance radius of $\delta_r = 0.002\,\mathrm{m}$ is used in the case of the tripped boundary layer flow. The same physical time step size $\Delta t = 7.1469 \cdot 10^{-5}$ ($= 400$ time steps per period at $k = 0.3$) is used in all computations. Therefore, the number of time steps per period is reduced for increasing frequency to obtain the same time step size. Five periods are computed for each reduced frequency to remove any transient behavior in the data. For the dual time stepping scheme, 500 inner iterations are used to converge each time step.

Fig. 22 shows the unsteady aerodynamic coefficients and the respective amplitude spectra obtained for the last pitch period for a reduced frequency of $k = 0.15$. The pitch amplitude of $\hat{\alpha} = 1\,\mathrm{deg}$ is rather large

for any aeroelastic consideration[5] as only the linear system response is used to determine the flutter onset of a wing, but the larger amplitude will introduce a more pronounced change in transition location to better demonstrate the effect on the boundary layer flow. Despite the large pitch amplitude, the system response in lift is quite linear as can be seen by the elliptic lift coefficient curve over angle of attack and by the dominance of the first harmonic in the lift coefficient amplitude spectra. Being more sensitive to changes in angle of attack, the unsteady moment and drag coefficients deviate stronger from a linear response.

The instantaneous skin friction coefficient distribution at four points I to IV, marked for the tripped computation in Fig. 22, are shown in Fig. 23. The respective points for the computation with free boundary layer transition are shown in Fig. 24. The turbulent wedges are present

---

[5] The pitch amplitude to determine the linear system response in a transonic flow is usually set to $\hat{\alpha} = 10^{-4}\,\mathrm{deg}$ or smaller.
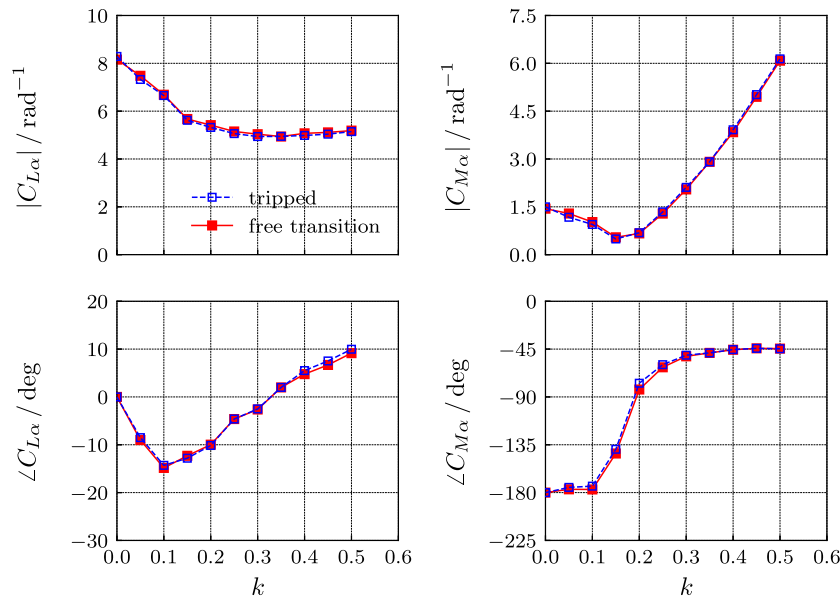
Fig. 25. Unsteady lift and moment coefficient for pitch motion computed with the DLR γ transition model.

during the whole pitch cycle and the transition location between the single wedges moves freely as the pressure gradient changes.

Fig. 25 shows the frequency-dependent unsteady lift and moment coefficient derivatives. The aerodynamic derivatives $C_{L\alpha}$ and $C_{M\alpha}$ are the transfer functions given by the Fourier-transformed system response C_L and C_M and the excitation α:

$$C_{L\alpha}(jk) = \frac{\text{FFT}\{C_L(t)\}}{\text{FFT}\{\alpha(t)\}}, \tag{13}$$

$$C_{M\alpha}(jk) = \frac{\text{FFT}\{C_M(t)\}}{\text{FFT}\{\alpha(t)\}}. \tag{14}$$

The values for quasi-steady flow at $k = 0$ are obtained for central differences of C_L and C_M at $\bar{\alpha} \pm 1$ deg. The phase information at $k = 0$ is given by the sign of the lift and moment curve slope.

The differences in $C_{L\alpha}$ and $C_{M\alpha}$ between the set-up with turbulent wedges on the upper surface of the wing and the polyline tripping on the lower surface (tripped) and the computation with free boundary layer transition are small. This holds for magnitude and phase of the transfer functions. These small differences despite the rather large difference in mean aerodynamics are already seen in Fig. 22 as the first harmonics of $|C_L|$ and $|C_M|$ are close to each other for both computational set-ups. This does not necessarily hold in general as previous experimental and numerical research has shown significant differences in the flutter behavior of airfoils with fully turbulent and transitional boundary layer flows [45].

4. Conclusion

This paper presents a method to include turbulent wedges and transition trippings in computations with correlation-based intermittency transport transition models. The transition model is solely disturbed at the wedge apex by setting the intermittency to $\gamma = 1$ within a certain disturbance radius and keeping the value throughout the solver run. The method can also be applied to include a tripping along a polyline. The method is tested for the CRM-NLF test case p2523. The turbulent wedges are successfully created, but the experimental turbulent wedge half-angles and orientation of the wedges are not met. The deficiencies remain despite changes in grid resolution, disturbance size, and diffusion coefficients and point at some basic flaws within these transition models. The experimental lift coefficient is met best for the tripped configuration with wedges on the upper surface and a polyline tripping on the lower wing surface. The experimental moment coefficient is in

better agreement with the computation that only includes the polyline tripping. It is assumed that the approach presented in this article is applicable to intermittency transport models in general.

Correlation-based models are usually set-up and calibrated based on two-dimensional test cases: a basic transition correlation is defined and intermittency production and destruction terms are weighted to obtain the right transition location downstream of the first intermittency increase. They form the necessary ad-hoc basis of the model but lack physical justification. The observation that these models are not able to reproduce the right three-dimensional transition behavior opens up new pathways to improve the correlation-based transition modeling approach. As shown, the turbulent wedge characteristics are Reynolds number dependent. Therefore, they depend on the specific development of the boundary layer, which locates them within the sphere of influence of the transition modeling approach. Returning to simple flat plate data on turbulent wedges with different pressure gradients might provide a fruitful path towards further model improvements. Especially complex three-dimensional flows would benefit by a more precise prediction of the intermittency transport and distribution. In addition, the turbulent wedge characteristics need to be investigated for different underlying turbulence models.

In addition to the numerical tests concerning the turbulent wedge angles, data are presented that show the specific effects of reduced laminarity on the steady and unsteady aerodynamics of the CRM-NLF configuration. Turbulent contamination in free flight may eventually decrease the fuel efficiency of a future active, passive, or hybrid laminar flow transport aircraft. A turbulent wedge model will support the thorough assessment of such a configuration: based on e.g. a set of Monte Carlo distributions of turbulent wedges, the actual drag benefit of a configuration might be compared to a clean configuration to better understand the net benefit of laminarity. Gaps and edges in the wing surface can be modeled by placing turbulent wedges at these known locations. To include numerical trippings in correlation-based models will result in more general applicable models. In addition, the effect of a localized loss of laminarity on e.g. control surfaces can be modeled. Such investigation will improve the understanding of certain aerodynamic and aeroelastic border-of-the-envelope effects for laminar wing configurations. This is especially the case as unsteady computations can readily be performed as shown for an oscillatory pitch motion in a transonic flow.

CRediT authorship contribution statement

Michael Fehrs: Writing – original draft, Investigation.

Declaration of competing interest

The authors declare that they have no known competing financial interests or personal relationships that could have appeared to influence the work reported in this paper.

Data availability

The authors do not have permission to share data.

References

[1] M. Fehrs, Boundary layer transition in external aerodynamics and dynamic aeroelastic stability, Ph.D. thesis, TU Braunschweig, Braunschweig, 2018.

[2] D.G. François, A. Krumbein, N. Krimmelbein, C. Grabe, Simplified stability-based transition transport modeling for unstructured computational fluid dynamics, J. Aircr. 60 (6) (2023) 1773–1784, https://doi.org/10.2514/1.C037163.

[3] F.R. Menter, P.E. Smirnov, T. Liu, R. Avancha, A one-equation local correlation-based transition model, Flow Turbul. Combust. 95 (4) (2015) 583–619, https://doi.org/10.1007/s10494-015-9622-4.

[4] J. Van den Eynde, J. Steelant, A. Passaro, Intermittency-based transition model with local empirical correlations, in: 21st AIAA International Space Planes and Hypersonics Technologies Conference, no. AIAA 2017-2378, AIAA, Xiamen, 2017.

[5] R. Djeddi, J.G. Coder, K. Ekici, Calibration of the critical amplification factor for Reynolds-averaged Navier–Stokes-based transition modeling, AIAA J. 60 (9) (2022) 5094–5108, https://doi.org/10.2514/1.J061476.

[6] P. Ströer, N. Krimmelbein, A. Krumbein, C. Grabe, Galilean-invariant stability-based transition transport modeling framework, AIAA J. 60 (7) (2022) 4126–4139, https://doi.org/10.2514/1.J061401.

[7] S. Helm, K. Davies, M. Fehrs, First comparison of cfd simulation and wind tunnel test of the forward-swept natural laminar flow model NLF-ECOWING-FSW, in: A. Dillmann, G. Heller, E. Krämer, C. Wagner, J. Weiss (Eds.), New Results in Numerical and Experimental Fluid Mechanics XIV, Springer Nature, Switzerland, Cham, 2024, pp. 425–434.

[8] C. Klein, U. Henne, Y. Deisuke, V. Ondruss, U. Beifuss, A.-K. Hensch, J. Quest, Application of carbon nanotubes and temperature sensitive paint for the detection of boundary layer transition under cryogenic conditions (invited), in: 55th AIAA Aerospace Sciences Meeting, no. AIAA 2017-0336, AIAA, Grapevine, 2017.

[9] S. Helm, M. Fehrs, C. Kaiser, N. Krimmelbein, A. Krumbein, Numerical simulation of the common research model with natural laminar flow, J. Aircr. 60 (2) (2023) 449–460, https://doi.org/10.2514/1.C036889.

[10] J. Neumann, D. Friedewald, H. Hennings, The influence of fixed transition modeling on aeroelastic simulations in comparison to wind tunnel experiments, CEAS Aeronaut. J. 9 (2018) 491–503, https://doi.org/10.1007/s13272-018-0299-y.

[11] A.C. Charters Jr., Transition Between Laminar and Turbulent Flow by Transverse Contamination, NACA-TN-891, NACA, 1943.

[12] G.B. Schubauer, P.S. Klebanoff, Contributions on the Mechanics of Boundary-Layer Transition, NACA-TR-1289, NACA, 1956.

[13] S. Zhong, T.P. Chong, H.P. Hodson, A comparison of spreading angles of turbulent wedges in velocity and thermal boundary layers, J. Fluids Eng. 125 (2) (2003) 267–274, https://doi.org/10.1115/1.1539871.

[14] J.P. Gostelow, N. Melwani, G.J. Walker, Effects of streamwise pressure gradient on turbulent spot development, J. Turbomach. 118 (4) (1996) 737–743, https://doi.org/10.1115/1.2840929.

[15] D. Goldstein, J. Chu, G. Brown, Lateral Spreading Mechanism of a Turbulent Spot and a Turbulent Wedge, Flow, Turbulence and Combustion, vol. 98, Springer, Cham, 2017, pp. 21–35.

[16] A.R. Berger, Fundamental mechanism of turbulent wedge spreading, Ph.D. thesis, Texas A&M University, College Station, 2020.

[17] M. Gad-El-Hak, R.F. Blackwelderf, J.J. Riley, On the growth of turbulent regions in laminar boundary layers, J. Fluid Mech. 110 (1981) 73–95, https://doi.org/10.1017/S002211208100061X.

[18] M. Fehrs, Boundary layer suction modeling based on the DLR TAU-Code effusion mass flux boundary condition, in: A. Dillmann, G. Heller, E. Krämer, C. Wagner, C. Tropea, S. Jakirlić (Eds.), New Results in Numerical and Experimental Fluid Mechanics XII, Springer, Cham, 2020, pp. 175–184.

[19] M. Fehrs, S. Helm, Turbulent wedge modeling in local correlation-based transition models, in: A. Dillmann, G. Heller, E. Krämer, C. Wagner, J. Weiss (Eds.), New Results in Numerical and Experimental Fluid Mechanics XIV, Springer Nature, Switzerland, Cham, 2024, pp. 415–424.

[20] M.N. Lynde, R.L. Campbell, Computational design and analysis of a transonic natural laminar flow wing for a wind tunnel model, in: 35th AIAA Applied Aerodynamics Conference, no. AIAA 2017-3058, AIAA, Denver, 2017.

[21] M.N. Lynde, R.L. Campbell, M.B. Rivers, S.A. Viken, D.T. Chan, A.N. Watkins, S.L. Goodliff, Preliminary results from an experimental assessment of a natural laminar flow design method, in: AIAA Scitech 2019 Forum, no. AIAA 2019-2298, AIAA, San Diego, 2019.

[22] M.N. Lynde, R.L. Campbell, S.A. Viken, Additional findings from the common research model natural laminar flow wind tunnel test, in: AIAA Aviation 2019 Forum, no. AIAA 2019-3292, AIAA, Dallas, 2019.

[23] N. Watkins, K.Z. Goodman, S. Peak, Transition detection at cryogenic temperatures using a carbon-based resistive heating layer coupled with temperature sensitive paint, in: AIAA Scitech 2019 Forum, no. AIAA 2019-2191, AIAA, San Diego, 2019.

[24] M.B. Rivers, M.N. Lynde, R.L. Campbell, S.A. Viken, D.T. Chan, A.N. Watkins, S.L. Goodliff, Experimental investigation of the NASA Common Research Model with a Natural Laminar Flow wing in the NASA Langley National Transonic Facility, in: AIAA Scitech 2019 Forum, no. AIAA 2019-2189, AIAA, San Diego, 2019.

[25] M. Rivers, Crm-nlf, https://commonresearchmodel.larc.nasa.gov/crm-nlf/. (Accessed 27 March 2023), 2022.

[26] M. Rivers, General information on the wind tunnel data from the crm-nlf test, version 2, https://commonresearchmodel.larc.nasa.gov/wp-content/uploads/sites/7/2020/02/CRM-NLF_Info_v2.pdf. (Accessed 27 March 2023), 2020.

[27] D. Schwamborn, T. Gerhold, R. Heinrich, The DLR TAU-Code: Recent applications in research and industry, in: ECCOMAS 2006, Delft, 2006.

[28] F.R. Menter, M. Kuntz, R. Langtry, Ten years of industrial experience with the SST turbulence model, in: K. Hanjalić, Y. Nagano, M. Tummers (Eds.), Turbulence, Heat and Mass Transfer 4, Begell House, Inc., Redding, 2003, pp. 625–632.

[29] R.C. Swanson, E. Turkel, On central-difference and upwind schemes, J. Comput. Phys. 101 (2) (1992) 292–306, https://doi.org/10.1016/0021-9991(92)90007-L.

[30] R. Dwight, Efficiency improvements of rans-based analysis and optimization using implicit and adjoint methods on unstructured grids, Ph.D. thesis, University of Manchester, Manchester, 2006.

[31] A. Jameson, Time dependent calculations using multigrid, with applications to unsteady flows past airfoils and wings, in: 10th Computational Fluid Dynamics Conference, no. AIAA 91-1596, AIAA, Honolulu, 1991, https://doi.org/10.2514/6.1991-1596.

[32] R.B. Langtry, F.R. Menter, Correlation-based transition modeling for unstructured parallelized computational fluid dynamics codes, AIAA J. 47 (12) (2009) 2894–2906, https://doi.org/10.2514/1.42362.

[33] D. Arnal, M. Habiballah, E. Coustols, Laminar instability theory and transition criteria in two and three-dimensional flow, Rech. Aérosp. 2 (1984) 45–63.

[34] J. Perraud, H. Deniau, G. Casalis, Overview of transition prediction tools in the elsA software, in: ECCOMAS 2014, Barcelona, 2014.

[35] H. Schlichting, K. Gersten, Boundary Layer Theory, 8th edition, Springer, Berlin, 2000.

[36] CentaurSoft, CENTAUR grid generator, https://www.centaursoft.com. (Accessed 16 March 2023), 2023.

[37] M. Rivers, Ntf test data, https://commonresearchmodel.larc.nasa.gov/crm-nlf/ntf-test-data/. (Accessed 13 April 2023), 2022.

[38] A. Krumbein, D.G. François, N. Krimmelbein, Transport-based transition prediction for the common research model natural laminar flow configuration, J. Aircr. 59 (6) (2022) 1562–1573, https://doi.org/10.2514/1.C036918.

[39] AIAA, 1st AIAA transition modeling and prediction workshop. Description of test cases, rev 1.2, https://transitionmodeling.larc.nasa.gov/wp-content/uploads/sites/109/2020/02/TransitionMPW_CaseDescriptions.pdf. (Accessed 13 April 2023), 2020.

[40] A. Krumbein, N. Krimmelbein, G. Schrauf, Automatic transition prediction in hybrid flow solver, part 1: methodology and sensitivities, J. Aircr. 46 (4) (2009) 1176–1190, https://doi.org/10.2514/1.39736.

[41] A. Krumbein, N. Krimmelbein, G. Schrauf, Automatic transition prediction in hybrid flow solver, part 2: practical application, J. Aircr. 46 (4) (2009) 1191–1199, https://doi.org/10.2514/1.39738.

[42] J.L. van Ingen, A suggested semi-empirical method for the calculation of the boundary layer transition region, Rapport VTH-74, TU Delft, 1956.

[43] J.L. Thomas, B. Diskin, C.L. Rumsey, Towards verification of unstructured-grid solvers, AIAA J. 46 (12) (2008) 3070–3079, https://doi.org/10.2514/1.36655.

[44] R.L. Bisplinghoff, H. Ashley, R.L. Halfman, Aeroelasticity, 1st edition, Dover Publications, Mineola, 1996.

[45] L. Tichy, H. Mai, M. Fehrs, J. Nitzsche, A. Hebler, Risk analysis for flutter of laminar wings, in: International Forum on Aeroelasticity and Structural Dynamics, no. IFASD-2017-196, IFASD, Como, 2017.